

# PLANET observations of microlensing event OGLE-1999-BUL-23: limb darkening measurement of the source star

M. D. Albrow<sup>1</sup>, J. An<sup>2</sup>, J.-P. Beaulieu<sup>3</sup>, J. A. R. Caldwell<sup>4</sup>, D. L. DePoy<sup>2</sup>,  
M. Dominik<sup>5</sup>, B. S. Gaudi<sup>2</sup>, A. Gould<sup>2</sup>, J. Greenhill<sup>6</sup>, K. Hill<sup>6</sup>, S. Kane<sup>6</sup>,  
R. Martin<sup>7</sup>, J. Menzies<sup>4</sup>, R. W. Pogge<sup>2</sup>, K. R. Pollard<sup>8</sup>, P. D. Sackett<sup>5</sup>,  
K. C. Sahu<sup>1</sup>, P. Vermaak<sup>4</sup>, R. Watson<sup>6</sup>, and A. Williams<sup>7</sup>

(The PLANET Collaboration)

## ABSTRACT

We present PLANET observations of OGLE-1999-BUL-23, a binary-lens microlensing event towards the Galactic bulge. PLANET observations in the I and V bands cover the event from just before the first caustic crossing until the end of the event. In particular, a densely-sampled second caustic crossing enables us to derive the linear limb-darkening coefficients of the source star;  $c_V = 0.786^{+0.080}_{-0.078}$  and  $c_I = 0.632^{+0.047}_{-0.037}$ . Combined analysis of the light curve and the color-magnitude diagram suggests that the source star is a G/K subgiant in the Galactic bulge ( $T_{\text{eff}} \simeq 4800$  K). The resulting linear limb-darkening coefficient of the source is consistent with theoretical predictions, although it is likely that non-linearity of the stellar surface brightness profile complicates the interpretation, especially for the I band. The global light curve fit to the data indicates that the event is due to a binary lens of a mass ratio  $q \simeq 0.39$  and a projected separation  $d \simeq 2.42$ . The lens/source relative proper motion is  $(22.8 \pm 1.5)$  km s<sup>-1</sup> kpc<sup>-1</sup>, typical of bulge/bulge or bulge/disk events.

*Subject headings:* binaries: general — gravitational microlensing — stars: atmospheres, fundamental parameters

---

<sup>1</sup>Space Telescope Science Institute, 3700 San Martin Drive, Baltimore, MD 21218, U.S.A.

<sup>2</sup>Ohio State University, Department of Astronomy, 140 W 18th Avenue, Columbus, OH 43210, U.S.A.

<sup>3</sup>Institut d'Astrophysique de Paris, INSU CNRS, 98 bis Boulevard Arago, F-75014, Paris, France

<sup>4</sup>South African Astronomical Observatory, P.O. Box 9, Observatory 7935, South Africa

<sup>5</sup>Kapteyn Astronomical Institute, Postbus 800, 9700 AV Groningen, The Netherlands

<sup>6</sup>University of Tasmania, Physics Department, G.P.O. 252C, Hobart, Tasmania 7001, Australia

<sup>7</sup>Perth Observatory, Walnut Road, Bickley, Western Australia 6076, Australia

<sup>8</sup>Univ. of Canterbury, Dept. of Physics & Astronomy, Private Bag 4800, Christchurch, New Zealand

## 1. Introduction

In point-source-point-lens (PSPL) microlensing events, the light curve yields only one physically interesting parameter, the characteristic time scale of the event,  $t_E$ , which is a combination of the mass of the lens and the source-lens relative parallax and proper motion. However, more varieties than PSPL events have been observed in reality, and using deviations from the standard light curve, one can deduce more information about the lens and the source. The Probing Lensing Anomalies NETWORK (PLANET) is an international collaboration that monitors events in search of such anomalous light curves using a network of telescopes in the southern hemisphere (Albrow et al. 1998).

One example of information that can be extracted from anomalous events is the surface brightness profile of the source star (Witt 1995). In a binary or multiple lens system, the caustic is an extended structure. If the source passes near or across the caustic, drastic changes in magnification near the caustics can reveal the finite size of the source (Gould 1994; Nemiroff & Wickramasinghe 1994; Witt & Mao 1994; Alcock et al. 1997), and one can even extract its surface-brightness profile (Bogdanov & Cherepashchuk 1996; Gould & Welch 1996; Sasselov 1997; Valls-Gabaud 1998).

The fall-off of the surface brightness near the edge of the stellar disk with respect to its center, known as limb darkening, has been extensively observed in the Sun. Theories of stellar atmospheres predict limb darkening as a general phenomenon and give models for different types of stars. Therefore, measurement of limb darkening in distant stars other than the Sun would provide important observational constraints on the study of stellar atmospheres. However, such measurements are very challenging with traditional techniques and have usually been restricted to relatively nearby stars or extremely large supergiants. As a result, only a few attempts have been made to measure limb darkening to date. The classical method of tracing the stellar surface brightness profile is the analysis of the light curves of eclipsing binaries (Wilson & Devinney 1971; Twigg & Rafert 1980). However, the current practice in eclipsing-binary studies usually takes the opposite approach to limb darkening (Claret 1998a) – constructing models of light curves using theoretical predictions of limb darkening. This came to dominate after Popper (1984) demonstrated that the uncertainty of limb darkening measurements from eclipsing binaries is substantially larger than the theoretical uncertainty. Since the limb-darkening parameter is highly correlated with other parameters of the eclipsing binary, fitting for limb darkening could seriously degrade the measurement of these other parameters. Multi-aperture interferometry and lunar occultation, which began as measurements of the angular sizes of stars, have also been used to resolve the surface structures of stars (Hofmann & Scholz 1998). In particular, a large wavelength dependence of the interferometric size of a stellar disk has been attributed to limb darkening, and higher order corrections to account for limb darkening have been widely

adopted in the interferometric angular size measurement of stars. Several recent investigations using optical interferometry extending beyond the first null of the visibility function have indeed confirmed that the observed patterns of the visibility function contradict a uniform stellar disk model and favor a limb-darkened disk (Quirrenbach et al. 1996; Hajian et al. 1998) although these investigations have used a model prediction of limb darkening inferred from the surface temperature rather than deriving the limb darkening from the observations. However, at least in one case, Burns et al. (1997) used interferometric imaging to measure the stellar surface brightness profile with coefficients beyond the simple linear model. In addition, developments of high resolution direct imaging in the last decade using space telescopes (Gilliland & Dupree 1996) or speckle imaging (Kluckers et al. 1997) have provided a more straightforward way of detecting stellar surface irregularities. However, most studies of this kind are still limited to a few extremely large supergiants, such as  $\alpha$  Ori. Furthermore, they seem to be more sensitive to asymmetric surface structures such as spotting than to limb darkening.

By contrast, microlensing can produce limb-darkening measurements for distant stars with reasonable accuracy. To date, limb darkening (more precisely, a set of coefficients of a parametrized limb-darkened profile) has been measured for source stars in three events, two K giants in the Galactic bulge and an A dwarf in the Small Magellanic Cloud (SMC). MACHO 97-BLG-28 was a cusp-crossing event of a K giant source with extremely good data, permitting Albrow et al. (1999a) to make a two-coefficient (linear and square-root) measurement of limb darkening. Afonso et al. (2000) used data from five microlensing collaborations to measure linear limb darkening coefficients in five filter bandpasses for MACHO 98-SMC-1, a metal-poor A star in the SMC. Although the data for this event were also excellent, the measurement did not yield a two-parameter determination because the caustic crossing was a fold-caustic rather than a cusp, and these are less sensitive to the form of the stellar surface brightness profile. Albrow et al. (2000a) measured a linear limb-darkening coefficient for MACHO 97-BLG-41, a complex rotating-binary event with both a cusp crossing and a fold-caustic crossing. In principle, such an event could give very detailed information about the surface brightness profile. However, neither the cusp nor the fold-caustic crossing was densely sampled, so only a linear parameter could be extracted.

In this paper, we report a new limb-darkening measurement of a star in the Galactic bulge by a fold-caustic crossing event, OGLE-1999-BUL-23, based on the photometric monitoring of PLANET.

## 2. OGLE-1999-BUL-23

OGLE-1999-BUL-23 was originally discovered towards the Galactic bulge by the Optical Gravitational Lensing Experiment (OGLE)<sup>9</sup> (Udalski et al. 1992; Udalski, Kubiak, & Szymański 1997). The PLANET collaboration observed the event as a part of our routine monitoring program after the initial alert, and detected a sudden increase in brightness on 12 June 1999.<sup>10</sup> Following this anomalous behavior, we began dense (typically one observation per hour) photometric sampling of the event. Since the source lies close to the (northern) winter solstice ( $\alpha = 18^h07^m45^s.14$ ,  $\delta = -27^\circ33'15''.4$ ), while the caustic crossing occurred nearly at the summer solstice (19 June 1999), and since good weather at all four of our southern sites prevailed throughout, we were able to obtain nearly continuous coverage of the second caustic crossing without any significant gaps. Visual inspection and initial analysis of the light curve revealed that the second crossing was due to a simple fold caustic crossing (see §2.2).

### 2.1. Data

We observed OGLE-1999-BUL-23 with I and V band filters at four participant telescopes: the Elizabeth 1 m at South African Astronomical Observatory (SAAO), Sutherland, South Africa; the Perth/Lowell 0.6 m telescope at Perth, Western Australia; the Canopus 1 m near Hobart, Tasmania, Australia; and the Yale/AURA/Lisbon/OSU 1 m at Cerro Tololo Inter-American Observatory (CTIO), La Serena, Chile. From June to August 1999 ( $1338 < \text{HJD}' < 1405$ ), PLANET obtained almost 600 images of the field of OGLE-1999-BUL-23. In addition, baseline points were taken at SAAO ( $\text{HJD}' \simeq 1440$ ) and Perth ( $\text{HJD}' \simeq 1450$ ;  $\text{HJD}' \simeq 1470$ ). Here  $\text{HJD}' \equiv \text{HJD} - 2450000$ , where HJD is Heliocentric Julian Date at center of exposure. The data reduction and photometric measurements of the event were performed relative to non-variable stars in the same field using DoPHOT. After several re-reductions, we recovered the photometric measurements from a total of 476 frames.

We assumed independent photometric systems for different observatories and thus explicitly included the determination of independent (unlensed) source and background fluxes for each different telescope and filter band in the analysis. This provides both determinations of the photometric offsets between different systems and independent estimates of the blending factors. The final results demonstrate satisfactory alignment among the data sets

---

<sup>9</sup>The OGLE alert for this event is posted at <http://www.astrouw.edu.pl/~ftp/ogle/ogle2/ews/bul-23.html>

<sup>10</sup>The PLANET anomaly and caustic alerts are found at <http://www.astro.rug.nl/~planet/OB99023cc.html>

(see §2.3), and we therefore believe that we have reasonable relative calibrations. Our previous studies have shown that the background flux (or blending factors) may correlate with the size of seeing disks in some cases (Albrow et al. 2000a,b). To check this, we introduced linear seeing corrections in addition to constant backgrounds.

From previous experience, it is expected that the formal errors reported by DoPHOT underestimate the actual errors (Albrow et al. 1998), and consequently that  $\chi^2$  is overestimated. Hence, we renormalize photometric errors to force the final reduced  $\chi^2/dof = 1$  for our best fit model. Here, *dof* is the number of degrees of freedom (the number of data points less the number of parameters). We determine independent rescaling factors for the photometric uncertainties from the different observatories and filters. The process involves two steps: the elimination of bad data points and the determination of error normalization factors. In this as in all previous events that we have analyzed, there are outliers discrepant by many  $\sigma$  that cannot be attributed to any specific cause even after we eliminate some points whose source of discrepancy is identifiable. Although, in principle, whether particular data points are faulty or not should be determined without any reference to models, we find that the light curves of various models that yield reasonably good fits to the data are very similar to one another, and furthermore, there is no indication of temporal clumping of highly discrepant points. We, therefore, identify outlier points with respect to our best model and exclude them from the final analysis.

For the determination of outliers, we follow an iterative approach using both steps of error normalization. First, we calculate the individual  $\chi^2$ 's of data sets from different observatories and filter bands with reference to our best model without any rejection or error scaling. Then, the initial normalization factors are determined independently for each data set using those individual  $\chi^2$ 's and the number of data points in each set. If the deviation of the most discrepant outlier is larger than what is predicted based on the number of points and the assumption of a normal distribution, we classify the point as bad and calculate the new  $\chi^2$ 's and the normalization factors again. We repeat this procedure until the largest outlier is comparable with the prediction of a normal distribution. Although the procedure appears somewhat arbitrary, the actual result indicates that there exist rather large decreases of  $\sigma$  between the last rejected and included data points. After rejection of bad points, 429 points remain (see Table 1 and Fig. 1).

## 2.2. Analysis: searching for $\chi^2$ minima

We use the method of Albrow et al. (1999b, hereafter Paper I), which was devised to fit the light curve of fold-caustic crossing binary-lens events, to analyze the light curve of this event and find an appropriate binary-lens solution. This method consists of three steps: (1)

fitting of caustic-crossing data using an analytic approximation of the magnification, (2) searching for  $\chi^2$  minima over the whole parameter space using the point-source approximation and restricted to the non-caustic crossing data, and (3)  $\chi^2$  minimization using all data and the full binary-lens equation in the neighborhood of the minima found in the second step.

For the first step, we fit the I-band caustic crossing data ( $1348.5 \leq \text{HJD}' \leq 1350$ ) to the six-parameter analytic curve shown in equation (1) that characterizes the shape of the second caustic crossing (Paper I; Afonso et al. 2000),

$$F(t) = \left(\frac{Q}{\Delta t}\right)^{1/2} \left[ G_0 \left(\frac{t - t_{cc}}{\Delta t}\right) + \Gamma H_{1/2} \left(\frac{t - t_{cc}}{\Delta t}\right) \right] + F_{cc} + (t - t_{cc}) \tilde{\omega}, \quad (1a)$$

$$G_n(\eta) \equiv \pi^{-1/2} \frac{(n+1)!}{(n+1/2)!} \int_{\max(\eta, -1)}^1 dx \frac{(1-x^2)^{n+1/2}}{(x-\eta)^{1/2}} \Theta(1-\eta), \quad (1b)$$

$$H_{1/2}(\eta) \equiv G_{1/2}(\eta) - G_0(\eta). \quad (1c)$$

Figure 2 shows the best-fit curve and the data points used for the fit. This caustic-crossing fit essentially constrains the search for a full solution to a four-dimensional hypersurface instead of the whole nine-dimensional parameter space (Paper I).

We construct a grid of point-source light curves with model parameters spanning a large subset of the hypersurface and calculate  $\chi^2$  for each model using the I-band non-caustic crossing data. After an extensive search for  $\chi^2$ -minima over the four-dimensional hypersurface, we find positions of two apparent local minima, each in a local valley of the  $\chi^2$ -surface. The smaller  $\chi^2$  of the two is found at  $(d, q, \alpha) \simeq (2.4, 0.4, 75^\circ)$ , where  $d$  is the projected binary separation in units of the Einstein ring radius,  $q$  is the mass ratio of the binary system, and  $\alpha$  is the angle between the binary axis and the path of the source, defined so that the geometric center of the lens system lies on the right hand side of the moving source. The other local minimum is  $(d, q, \alpha) \simeq (0.55, 0.55, 260^\circ)$ . The results appear to suggest a rough symmetry of  $d \leftrightarrow d^{-1}$  and  $(\alpha < \pi) \leftrightarrow (\alpha > \pi)$ , as was found for MACHO 98-SMC-1 (Paper I; Afonso et al. 2000). Besides these two local minima, there are several isolated  $(d, q)$ -grid points at which  $\chi^2$  is smaller than at neighboring grid points. However, on a finer grid they appear to be connected with one of the two local minima specified above. We include the two local minima and some of the apparently isolated minimum points as well as points in the local valley around the minima as starting points for the refined search of  $\chi^2$ -minimization in the next step.

### 2.3. Solutions: $\chi^2$ minimization

Starting from the local minima found in §2.2 and the points in the local valleys around them, we perform a refined search for the  $\chi^2$  minimum. The  $\chi^2$  minimization includes all the I and V data points for successive fitting to the full expression for magnification, accounting for effects of a finite source size and limb darkening.

As described in Paper I, the third step makes use of a variant of equation (1) to evaluate the magnified flux in the neighborhood of the caustic crossing. Paper I found that, for MACHO 98-SMC-1, this analytic expression was an extremely good approximation to the results of numerical integration and assumed that the same would be the case for any fold crossing. Unfortunately, we find that, for OGLE-1999-BUL-23, this approximation deviates from the true magnification as determined using the method of Gould & Gaucherel (1997) as much as 4%, which is larger than our typical photometric uncertainty in the region of caustic crossing. To maintain the computational efficiency of Paper I, we continue to use the analytic formula (1), but correct it by pre-tabulated amounts given by the fractional difference (evaluated close to the best solution) between this approximation and the values found by numerical integration. We find that this correction works quite well even at the local minimum for the other (close-binary) solution – the error is smaller than 1%, and in particular, the calculations agree within 0.2% for the region of primary interest. The typical (median) photometric uncertainties for the same region are 0.015 mag (Canopus after the error normalization) and 0.020 mag (Perth). In addition, we test the correction by running the fitting program with the exact calculation at the minimum found using the corrected approximation, and find that the measured parameters change less than the precision of the measurement. In particular, the limb-darkening coefficients change by an order of magnitude less than the measurement uncertainty due to the photometric errors.

The results of the refined  $\chi^2$  minimization are listed in Table 2 for three discrete “solutions” and in Table 3 for grid points neighboring the best-fit solution whose  $\Delta\chi^2$  is less than one. The first seven columns describe seven of the standard parameters of the binary-lens model (the remaining two parameters are the source and background flux). The eighth column is the time of the second caustic crossing ( $t_{cc}$ ) – the time when the center of the source crossed the caustic. The limb darkening coefficients for I and V bands are shown in the next two columns. The final column is  $\Delta\chi^2$ ,

$$\Delta\chi^2 \equiv \frac{\chi^2 - \chi_{\text{best}}^2}{\chi_{\text{best}}^2/dof}, \quad (2)$$

as in Paper I. The light curve (in magnification) of the best-fit model is shown in Figure 3 together with all the data points used in the analysis.

### 2.3.1. “Degeneracy”

For typical binary-lens microlensing events, more than one solution often fits the observations reasonably well. In particular, Dominik (1999) predicted a degeneracy between close and wide binary lenses resulting from a symmetry in the lens equation itself, and such a degeneracy was found empirically for MACHO 98-SMC-1 (Paper I; Afonso et al. 2000).

We also find two distinct local  $\chi^2$  minima (§2.2) that appear to be closely related to such degeneracies. However, in contrast to the case of MACHO 98-SMC-1, our close-binary model for OGLE-1999-BUL-23 has substantially higher  $\chi^2$  than the wide-binary model ( $\Delta\chi^2 = 127.86$ ). Figure 4 shows the predicted light curves in SAAO instrumental I band. The overall geometries of these two models are shown in Figures 5 and 6. The similar morphologies of the caustics with respect to the path of the source is responsible for the degenerate light curves near the caustic crossing (Fig. 6). However, the close-binary model requires a higher blending fraction and lower baseline flux than the wide-binary solution because the former displays a higher peak magnification ( $A_{\max} \sim 50$  vs.  $A_{\max} \sim 30$ ). Consequently, a precise determination of the baseline can significantly contribute to discrimination between the two models, and in fact, the actual data did constrain the baseline well enough to produce a large difference in  $\chi^2$ .

A fair number of pre-event baseline measurements are available via OGLE, and those data can further help discriminate between these two “degenerate” models. We fit OGLE measurements to the two models with all the model parameters being fixed and allowing only the baseline and the blending fraction as free parameters. We find that the PLANET wide-binary model produces  $\chi^2 = 306.83$  for 169 OGLE points ( $\chi^2/dof = 1.83$ , compare Table 1) while  $\chi^2 = 608.22$  for the close-binary model for the same 169 points (Fig. 7). That is,  $\Delta\chi^2 = 164.04$ , so that the addition of OGLE data by itself discriminates between the two models approximately as well as all the PLANET data combined. The largest contribution to this large  $\Delta\chi^2$  appears to come from the period about a month before the first caustic crossing which is well covered by the OGLE data but not by the PLANET data. In particular, the close-binary model predicts a bump in the light curve around  $HJD' \simeq 1290$  due to a triangular caustic (see Fig. 5), but the data do not show any abnormal feature in the same region, although it is possible that rotation of the binary moved the caustic far from the source trajectory (eg. Afonso et al. 2000). In brief, the OGLE data strongly favor the wide-binary model.

### 2.3.2. Limb-Darkening Coefficients

The limb darkening of the source is parametrized using a normalized linear model of the source surface brightness profile, which was introduced in Appendix B of Paper I,

$$S_\lambda(\vartheta) = \bar{S}_\lambda \left[ 1 - \Gamma_\lambda \left( 1 - \frac{3}{2} \cos \vartheta \right) \right] = \bar{S}_\lambda \left[ (1 - \Gamma_\lambda) + \frac{3}{2} \Gamma_\lambda \cos \vartheta \right],$$

where  $\sin \vartheta \equiv \frac{\theta}{\theta_*}$  and  $\bar{S}_\lambda \equiv \frac{F_{s,\lambda}}{\pi \theta_*^2}$ , (3)

while linear limb darkening is usually parametrized by,

$$S_\lambda(\vartheta) = S_\lambda(0) [1 - c_\lambda (1 - \cos \vartheta)] = S_\lambda(0) [(1 - c_\lambda) + c_\lambda \cos \vartheta]. \quad (4)$$

The relationship between the two expressions of linear limb-darkening coefficients is

$$c_\lambda = \frac{3\Gamma_\lambda}{2 + \Gamma_\lambda}. \quad (5)$$

Amongst our six data sets, data from SAAO did not contain points that were affected by limb darkening, i.e. caustic crossing points. Since the filters used at different PLANET observatories do not differ significantly from one another, we use the same limb-darkening coefficient for the three remaining I-band data sets. The V-band coefficient is determined only from Canopus data, so that a single coefficient is used automatically.

For the best-fit lens geometry, the measured values of linear limb-darkening coefficients are  $\Gamma_I = 0.534 \pm 0.020$  and  $\Gamma_V = 0.711 \pm 0.089$ , where the errors include only uncertainties in the linear fit due to the photometric uncertainties at *fixed* binary-lens model parameters. However, these errors underestimate the actual uncertainties of the measurements because the measurements are correlated with the determination of the seven lens parameters shown in Tables 2 and 3. Incorporating these additional uncertainties in the measurement (see the next section for a detailed discussion of the error determination), our final estimates are

$$\Gamma_I = 0.534_{-0.040}^{+0.050} \quad (c_I = 0.632_{-0.037}^{+0.047}), \quad (6a)$$

$$\Gamma_V = 0.711_{-0.095}^{+0.098} \quad (c_V = 0.786_{-0.078}^{+0.080}). \quad (6b)$$

This is consistent with the result of the caustic-crossing fit of §2.2 ( $\Gamma_I = 0.519 \pm 0.043$ ). Our result suggests that the source is more limb-darkened in *V* than in *I*, which is generally expected by theories. Figure 8 shows the I-band residuals (in magnitudes) at the second caustic crossing from our best-fit models for a linearly limb-darkened and a uniform disk model. It is clear that the uniform disk model exhibits larger systematic residuals near the peak than the linearly limb-darkened disk. From the residual patterns – the uniform disk

model produces a shallower slope for the most of the falling side of the second caustic crossing than the data require, one can infer that the source should be more centrally concentrated than the model predicts, and consequently the presence of limb darkening. The linearly limb-darkened disk reduces the systematic residuals by a factor of  $\sim 5$ . Formally, the difference of  $\chi^2$  between the two models is 172.8 with two additional parameters for the limb-darkened disk model, i.e. the data favor a limb-darkened disk over a uniform disk at very high confidence.

### 3. Error Estimation for Limb Darkening Coefficients

Due to the multi-parameter character of the fit, a measurement of any parameter is correlated with other parameters of the model. The limb-darkening coefficients obtained with the different model parameters shown in Table 3 exhibit a considerable scatter, and in particular, for the I-band measurement, the scatter is larger than the uncertainties due to the photometric errors. This indicates that, in the measurement of the limb-darkening coefficients, we need to examine errors that correlate with the lens model parameters in addition to the uncertainties resulting from the photometric uncertainties at fixed lens parameters. This conclusion is reinforced by the fact that the error in the estimate of  $\Gamma$  from the caustic-crossing fit (see Fig. 2), which includes the correlation with the parameters of the caustic-crossing, is substantially larger than the error in the linear fit, which does not.

Since limb darkening manifests itself mainly around the caustic crossing, its measurement is most strongly correlated with  $\Delta t$  and  $t_{cc}$ . To estimate the effects of these correlations, we fit the data to models with  $\Delta t$  or  $t_{cc}$  fixed at several values near the best fit – the global geometry of the best fit, i.e.  $d$  and  $q$  being held fixed as well. The resulting distributions of  $\Delta\chi^2$  have parabolic shapes as a function of the fit values of the limb-darkening coefficient and are centered at the measurement of the best fit. (Both,  $\Delta t$  fixed and  $t_{cc}$  fixed, produce essentially the same parabola, and therefore, we believe that the uncertainty related to each correlation with either  $\Delta t$  or  $t_{cc}$  is, in fact, same in its nature.) We interpret the half width of the parabola at  $\Delta\chi^2 = 1$  ( $\delta\Gamma_I = 0.031$ ,  $\delta\Gamma_V = 0.032$ ) as the uncertainty due to the correlation with the caustic-crossing parameters at a given global lens geometry of a fixed  $d$  and  $q$ .

Although the global lens geometry should not *directly* affect the limb darkening measurement, the overall correlation between local and global parameters can contribute an additional uncertainty to the measurement. This turns out to be the dominant source of the scatter found in Table 3. To incorporate this into our final determination of errors, we examine the varying range of the measured coefficients over  $\Delta\chi^2 \leq 1$ . The result is

apparently asymmetric between the direction of increasing and decreasing the amounts of limb darkening. We believe that this is real, and thus we report asymmetric error bars for the limb-darkening measurements.

The final errors of the measurements reported in §2.3.2 are determined by adding these two sources of error to the photometric uncertainty in quadrature. The dominant source of errors in the I-band coefficient measurement is the correlation between the global geometry and the local parameters whereas the photometric uncertainty is the largest contribution to the uncertainties in the V-band coefficient measurement.

Although the measurements of V and I band limb darkening at fixed model parameters are independent, the final estimates of two coefficients are not actually independent for the same reason discussed above. (The correlation between V and I limb-darkening coefficients is clearly demonstrated in Table 3.) Hence, the complete description of the uncertainty requires a covariance matrix.

$$C = C_{\text{phot}} + \tilde{C}_{\text{cc}}^{1/2} \begin{pmatrix} 1 & \xi \\ \xi & 1 \end{pmatrix} \tilde{C}_{\text{cc}}^{1/2} + \tilde{C}_{\text{geom}}^{1/2} \begin{pmatrix} 1 & \xi \\ \xi & 1 \end{pmatrix} \tilde{C}_{\text{geom}}^{1/2}, \quad (7a)$$

$$C_{\text{phot}} \equiv \begin{pmatrix} \sigma_{V,\text{phot}}^2 & 0 \\ 0 & \sigma_{I,\text{phot}}^2 \end{pmatrix}, \quad (7b)$$

$$\tilde{C}_{\text{cc}}^{1/2} \equiv \begin{pmatrix} \sigma_{V,\text{cc}} & 0 \\ 0 & \sigma_{I,\text{cc}} \end{pmatrix}, \quad (7c)$$

$$\tilde{C}_{\text{geom}}^{1/2} \equiv \begin{pmatrix} \bar{\sigma}_{V,\text{geom}} & 0 \\ 0 & \bar{\sigma}_{I,\text{geom}} \end{pmatrix}, \quad (7d)$$

where the subscript (phot) denotes the uncertainties due to the photometric errors; (cc), the correlation with  $\Delta t$  and  $t_{\text{cc}}$  at a fixed  $d$  and  $q$ ; (geom), the correlation with the global geometry, and  $\xi$  is the correlation coefficient between  $\Gamma_V$  and  $\Gamma_I$  measurement. We derive the correlation coefficient using each measurement of  $\Gamma_V$  and  $\Gamma_I$ , and the result indicates that two measurements are almost perfectly correlated ( $\xi = 0.995$ ). We accommodate asymmetry of the errors by making the error ellipse off-centered with respect to the best estimate. (See §5 for more discussion on the error ellipses.)

#### 4. Physical Properties of the Source Star

Figure 9 shows color-magnitude diagrams (CMDs) derived from a  $2' \times 2'$  SAAO field and a  $4' \times 4'$  Canopus field centered on OGLE-1999-BUL-23 with positions marked for

the unmagnified source (S), the baseline (B), blended light (BL) at median seeing, and the center of red clump giants (RC). The source position in these CMDs is consistent with a late G or early K subgiant in the Galactic bulge (see below). Using the color and magnitude of red clump giants in the Galactic bulge reported by Pacyński et al. (1999) ( $I_{\text{RC}} = 14.37 \pm 0.02$ ,  $[V - I]_{\text{RC}} = 1.114 \pm 0.003$ ), we measure the reddening-corrected color and magnitude of the source in the Johnson-Cousins system from the relative position of the source with respect to the center of red clump in our CMDs, and obtain:

$$(V - I)_{\text{S},0} = 1.021 \pm 0.044, \quad (8a)$$

$$V_{\text{S},0} = 18.00 \pm 0.06, \quad (8b)$$

where the errors include the difference of the source positions in the two CMDs, but may still be somewhat underestimated because the uncertainty in the selection of red clump giants in our CMDs has not been quantified exactly.

From this information, we derive the surface temperature of the source;  $T_{\text{eff}} = (4830 \pm 100)$  K, using the color calibration in Bessell, Castelli, & Plez (1998) and assuming  $\log g = 3.5$  and the solar abundance. This estimate of temperature is only weakly dependent on the assumed surface gravity and different stellar atmospheric models. To determine the angular size of the source, we use equation (4) of Albrow et al. (2000a), which is derived from the surface brightness-color relation of van Belle (1999). We first convert  $(V - I)_{\text{S},0}$  into  $(V - K)_{\text{S},0} = 2.298 \pm 0.113$  using the same color calibration of Bessell et al. (1998) and then obtain the angular radius of the source of

$$\begin{aligned} \theta_* &= (1.86 \pm 0.13) \mu\text{as} \\ &= (0.401 \pm 0.027) R_{\odot} \text{ kpc}^{-1}. \end{aligned} \quad (9)$$

If the source is at the Galactocentric distance (8 kpc), this implies that the radius of the source is roughly  $3.2R_{\odot}$ , which is consistent with the size of a  $\sim 1M_{\odot}$  subgiant ( $\log g = 3.4$ ).

Combining this result with the parameters of the best-fit model yields

$$\begin{aligned} \mu = \theta_*/(\Delta t \sin \phi) &= (13.2 \pm 0.9) \mu\text{as day}^{-1} \\ &= (22.8 \pm 1.5) \text{ km s}^{-1} \text{ kpc}^{-1}, \end{aligned} \quad (10)$$

$$\theta_{\text{E}} = \mu t_{\text{E}} = (0.634 \pm 0.043) \text{ mas}, \quad (11)$$

where  $\phi = 123^{\circ}9$  is the angle that the source crosses the caustic (see Fig. 6). This corresponds to a projected relative velocity of  $(182 \pm 12) \text{ km s}^{-1}$  at the Galactocentric distance, which is generally consistent with what is expected in typical bulge/bulge or bulge/disk (source/lens) events, but inconsistent with disk/disk lensing. Hence we conclude that the

source is in the bulge. As for properties of the lens, the projected separation of the binary lens is  $(1.53 \pm 0.10)$  AU  $\text{kpc}^{-1}$ , and the combined mass of the lens is given by

$$M_L = \frac{c^2 D_S D_L}{4G(D_S - D_L)} \theta_E^2 = (0.395 \pm 0.053) \left( \frac{x}{1-x} \right) \left( \frac{D_S}{8 \text{ kpc}} \right) M_\odot, \quad (12)$$

where  $x \equiv D_L/D_S$ ,  $D_L$  is the distance to the lens, and  $D_S$  is the distance to the source.

## 5. Limb Darkening of the Source

We compare our determination of the linear limb-darkening coefficients to model calculations by Claret, Díaz-Cordovés, & Giménez (1995) and Díaz-Cordovés, Claret, & Giménez (1995). For an effective temperature of  $T_{\text{eff}} = (4830 \pm 100)$  K and a surface gravity of  $\log g = 3.5$ , the interpolation of the V-band linear limb-darkening coefficients,  $c_V$ , of Díaz-Cordovés et al. (1995) predicts a value  $c_V = 0.790 \pm 0.012$ , very consistent with our measurement. However, for the I-band coefficient, the prediction of Claret et al. (1995),  $c_I = 0.578 \pm 0.008$ , is only marginally consistent with our measurement, at the  $1.46 \sigma$  level. Adopting a slightly different gravity does not qualitatively change this general result. Since we believe that the uncertainty in the color of the source is larger than in the limb-darkening coefficients, we also examine the opposite approach to the theoretical calculations – using the measured values of limb-darkening coefficients to derive the effective temperature of the source. If the source is a subgiant ( $\log g \simeq 3.5$ ) as our CMDs suggest, the measured values of the limb-darkening coefficients are expected to be observed in stars of the effective temperature,  $T_{\text{eff}} = (4850_{-670}^{+650})$  K for  $c_V$  or  $T_{\text{eff}} = (4200_{-490}^{+390})$  K for  $c_I$ . As before, the estimate from the V-band measurement shows a better agreement with the measured color than the estimate from the I-band. Considering that the data quality of I band is better than V band (the estimated uncertainty is smaller in  $I$  than in  $V$ ), this result needs to be explained.

In Figure 10, we plot theoretical calculations of  $(c_I, c_V)$  together with our measured values. In addition to Díaz-Cordovés et al. (1995) and Claret et al. (1995) (A), we also include the calculations of linear limb-darkening coefficients by van Hamme (1993) (B) and Claret (1998b) (C). For all three calculations, the V-band linear coefficients are generally consistent with the measured coefficients and the color, although van Hamme (1993) predicts a slightly smaller amount of limb darkening than the others. On the other hand, the calculations of the I-band linear coefficients are somewhat smaller than the measurement except for Claret (1998b) with  $\log g = 4.0$ . (However, to be consistent with a higher surface gravity while maintaining its color, the source star should be in the disk, which is inconsistent with our inferred proper motion.) Since  $c_V$  and  $c_I$  are not independent (in

both the theories and in our measurement), it is more reasonable to compare the I and V band measurements to the theories simultaneously. Using the covariance matrix of the measurement of  $\Gamma_I$  and  $\Gamma_V$  (see §3), we derive error ellipses for our measurements in the  $(c_I, c_V)$  plane and plot them in Figure 10. Formally, at the  $1\sigma$  level, the calculations of the linear limb-darkening coefficients in any of these models are not consistent with our measurements. In principle, one could also constrain the most likely stellar types that are consistent with the measured coefficients, independent of *a priori* information on the temperature and the gravity, with a reference to a model. If we do this, the result suggests either that the surface temperature is cooler than our previous estimate from the color or that the source is a low-mass main-sequence ( $\log g \geq 4.0$ ) star. However, the resulting constraints are not strong enough to place firm limits on the stellar type even if we assume any of these models to be “correct”.

One possible explanation of our general result – the measured V-band coefficients are nearly in perfect agreement with theories while the I-band coefficients are only marginally consistent – is non-linearity of stellar limb darkening. Many authors have pointed out the inadequacy of the linear limb darkening in producing a reasonably high-accuracy approximation of the real stellar surface brightness profile (Wade & Rucinski 1985; Díaz-Cordovés & Giménez 1992; van Hamme 1993; Claret 1998b). Indeed, Albrow et al. (1999a) measured the two-coefficient square-root limb darkening for a cusp-crossing microlensing event and found that the single-coefficient model gives a marginally poorer fit to the data. The quality of the linear parameterization has been investigated for most theoretical limb-darkening calculations, and the results seem to support this explanation. van Hamme (1993) defined the quality factors (Q in his paper) for his calculations of limb-darkening coefficients, and for  $4000 \text{ K} \leq T_{\text{eff}} \leq 5000 \text{ K}$  and  $3.0 \leq \log g \leq 4.0$ , his results indicate that the linear parameterization is a better approximation for V band than for I band. Similarly, Claret (1998b) provided plots of summed residuals ( $\sigma$  in his paper) for his fits used to derive limb-darkening coefficients showing that the V-band linear limb-darkening has lower  $\sigma$  than I-band and is as good as the V-band square-root limb-darkening near the temperature range of our estimate for the source of OGLE-1999-BUL-23. In fact, Díaz-Cordovés et al. (1995) reported that the V-band limb darkening is closest to the linear law in the temperature range  $T_{\text{eff}} = 4500 \sim 4750 \text{ K}$ . In summary, the source happens to be very close to the temperature at which the linear limb darkening is a very good approximation in V, but is less good in I.

The actual value of the coefficient in the linear parameterization of a non-linear profile may vary depending on the method of calculation and sampling. In order to determine the linear coefficients, models (A) and (C) used a least square fit to the theoretical (non-parametric) profile by sampling uniformly over  $\cos \vartheta$  (see eq. [3]), while model (B) utilized

the principle of total flux conservation between parametric and non-parametric profiles. On the other hand, a fold-caustic crossing event samples the stellar surface brightness by convolving it with a rather complicated magnification pattern (Gaudi & Gould 1999). Therefore, it is very likely that neither of the above samplings and calculations is entirely suitable for the representation of the limb-darkening measurement by microlensing unless the real intensity profile of the star is actually same as the assumed parametric form (the linear parameterization, in this case). In fact, the most appropriate way to compare the measurement to the stellar atmospheric models would be a direct fit to the (non-parametric) theoretical profile after convolution with the magnification patterns near the caustics. In the present paper, this has not been done, but we hope to make such a direct comparison in the future.

We thank A. Udalski for re-reducing the OGLE data on very short notice after we noticed an apparent discrepancy between the PLANET data and the original OGLE reductions. This work was supported by grants AST 97-27520 and AST 95-30619 from the NSF, by grant NAG5-7589 from NASA, by a grant from the Dutch ASTRON foundation through ASTRON 781.76.018, by a Marie Curie Fellowship from the European Union, and by “coup de pouce 1999” award from the Ministère de l’Éducation nationale, de la Recherche et de la Technologie.

## REFERENCES

- Afonso, C. et al. 2000, *ApJ*, 532, 340
- Albrow, M.D. et al. 1998, *ApJ*, 509, 687
- Albrow, M.D. et al. 1999a, *ApJ*, 522, 1011
- Albrow, M.D. et al. 1999b, *ApJ*, 522, 1022 (Paper I)
- Albrow, M.D. et al. 2000a, *ApJ*, 534, 894
- Albrow, M.D. et al. 2000b, *ApJ*, 535, 176
- Alcock, C. et al. 1997, *ApJ*, 491, 436
- Bessell, M.S., Castelli, F., & Plez, B. 1998, *A&A*, 333, 231
- Bogdanov, M.B. & Cherepashchuk, A.M. 1996, *Astron. Rep.*, 40, 713
- Burns, D. et al. 1997, *MNRAS*, 209, L11

- Claret, A. 1998a, A&AS, 131, 395
- Claret, A. 1998b, A&A, 335, 647
- Claret, A., Díaz-Cordovés, J., & Giménez, A. 1995, A&AS, 114, 247
- Díaz-Cordovés, J. & Giménez, A. 1992, A&A, 259, 227
- Díaz-Cordovés, J., Claret, A., & Giménez, A. 1995, A&AS, 110, 329
- Dominik, M. 1999, A&A, 349, 108
- Gaudi, B.S. & Gould, A. 1999, ApJ, 513, 619
- Gilliland, R.L. & Dupree, A.K. 1996, ApJ, 463, L29
- Gould, A. 1994, ApJ, 421, L71
- Gould, A. & Gaucherel, C. 1997, ApJ, 477, 580
- Gould, A. & Welch, D.L. 1996, ApJ, 464, 212
- Hajian, A.R. et al. 1998, ApJ, 496, 484
- Hofmann, K.-H. & Scholz, M. 1998, A&A, 335, 637
- Kluckers, V.A., Edmunds, M.G., Morris, R.H., & Wooder, N. 1997, MNRAS, 284, 711
- Nemiroff, R.J., & Wickramasinge, W.A.D.T 1994, ApJ, 424, L21
- Pacyński, B., Udalski, A., Szymański, M., Kubiak, M., Pietrzyński, I., Woźniak, P., & Żebruń, K. 1999, Acta Astron., 49, 319
- Popper, D.M. 1984, AJ, 89, 132
- Quirrenbach, A., Mozurkewich, D., Buscher, D.F., Hummel, C.A., & Armstrong, J.T. 1996, A&A, 312, 160
- Sasselov, D.D. 1997, in IAP Colloq. Proc. 12, Variable Stars and the Astrophysical Returns of Microlensing Surveys, eds. R. Ferlet, J.-P. Maillard, & B. Raban (Cedex: Editions Frontieres), 141
- Twigg, L.W. & Rafert, J.B. 1980, MNRAS, 193, 773
- Udalski, A., Kubiak, M. & Szymański, M. 1997, Acta Astron., 47, 319
- Udalski, A., Szymański, M., Kaluzny, J., Kubiak, M., & Mateo M. 1992, Acta Astron., 42, 253

- Valls-Gaubaud, D. 1998, MNRAS, 294, 747
- van Belle, G.T. 1999, PASP, 111, 1515
- van Hamme, W. 1993, AJ, 106, 2096
- Wade, R.A. & Rucinski, S.M. 1985, A&AS, 60, 471
- Wilson, R.E. & Devinney, E.J. 1971, ApJ, 166, 605
- Witt, H.J. 1995, ApJ, 449, 42
- Witt, H.J. & Mao, S. 1994, ApJ, 430, 505

Table 1. PLANET photometry of OGLE-1999-BUL-23

telescope	filter	# points	normalization <sup>a</sup>	$b_m$ <sup>b</sup> (%)	$\hat{\eta}$ <sup>c</sup> (arcsec <sup>-1</sup> )	$\theta_m$ <sup>d</sup> (arcsec)
SAAO	<i>I</i>	106	1.55	66.65	0.0389	1.702
	<i>V</i>	47	2.27	98.65	0.2136	1.856
Perth	<i>I</i>	39	1.00	81.26	0	2.080
Canopus	<i>I</i>	99	1.92	59.93	-0.1376	2.527
	<i>V</i>	35	1.88	92.06	-0.7626	2.587
CTIO	<i>I</i>	103	1.44	41.14	0.1794	1.715

<sup>a</sup> $\sigma_{\text{normalized}} = (\text{normalization}) \times \sigma_{\text{DoPHOT}}$

<sup>b</sup>Blending fraction at median seeing,  $b_m \equiv (F_{B,0} + \eta\theta_m)/F_S$

<sup>c</sup>Scaled seeing correction coefficient,  $\hat{\eta} \equiv \eta/F_S$

<sup>d</sup>Median seeing disk size in FWHM

Note. — The predicted flux of magnified source is  $F = F_S A + F_{B,0} + \eta\theta = F_S [A + b_m + \hat{\eta}(\theta - \theta_m)]$ , where  $A$  is magnification and  $\theta$  is the FWHM of the seeing disk in arcsec. The values of  $b_m$  and  $\hat{\eta}$  are evaluated for the best model (wide w/LD), in Table 2.

Table 2. PLANET solutions for OGLE-1999-BUL-23

$d$	$q$	$\alpha^a$ (deg)	$u_0^b$	$\rho_*$ ( $\times 10^{-3}$ )	$t_E$ (days)	$t_0^b$ (HJD') <sup>c</sup>	$t_{cc}$ (HJD') <sup>c</sup>	$\Gamma_I$	$\Gamma_V$	$\Delta\chi^2$	note
2.42	0.39	74.63	0.90172	2.941	48.20	1356.154	1349.1062	0.534	0.711	0.000	wide w/LD <sup>d</sup>
0.56	0.56	260.35	0.10052	2.896	34.20	1344.818	1349.1063	0.523	0.693	127.863	close w/LD
2.43	0.40	74.65	0.90987	2.783	48.48	1356.307	1349.1055	0.	0.	172.815	wide no-LD

<sup>a</sup>The lens system is on the right-hand side of the moving source.

<sup>b</sup>the closest approach to the midpoint of the lens system

<sup>c</sup>HJD'  $\equiv$  HJD  $-$  2450000.

<sup>d</sup>LD  $\equiv$  Limb Darkening

Table 3. Models in the neighborhood of the best-fit solution

$d$	$q$	$\alpha$ (deg)	$u_0$	$\rho_*$ ( $\times 10^{-3}$ )	$t_E$ (days)	$t_0$ (HJD')	$t_{cc}$ (HJD')	$\Gamma_I$	$\Gamma_V$	$\Delta\chi^2$
2.40	0.39	74.68	0.89020	2.998	47.41	1355.767	1349.1064	0.560	0.730	0.616
2.41	0.38	74.59	0.89362	2.955	47.94	1356.010	1349.1062	0.529	0.707	0.839
2.41	0.39	74.66	0.89587	2.968	47.80	1355.961	1349.1062	0.533	0.709	0.481
2.41	0.40	74.72	0.89832	2.981	47.68	1355.909	1349.1065	0.567	0.736	0.488
2.42	0.38	74.51	0.89912	2.930	48.37	1356.255	1349.1061	0.522	0.701	0.474
<b>2.42</b>	<b>0.39</b>	74.63	0.90172	2.941	48.20	1356.154	1349.1062	<b>0.534</b>	<b>0.711</b>	<b>0.000</b>
2.42	0.40	74.68	0.90407	2.954	48.09	1356.111	1349.1065	0.566	0.736	0.618
2.43	0.38	74.48	0.90489	2.904	48.78	1356.460	1349.1062	0.523	0.702	0.612
2.43	0.39	74.62	0.90754	2.913	48.60	1356.335	1349.1061	0.529	0.706	0.666
2.43	0.40	74.66	0.90974	2.923	48.48	1356.300	1349.1062	0.532	0.709	0.916
2.44	0.39	74.54	0.91312	2.888	49.03	1356.580	1349.1062	0.532	0.710	0.602

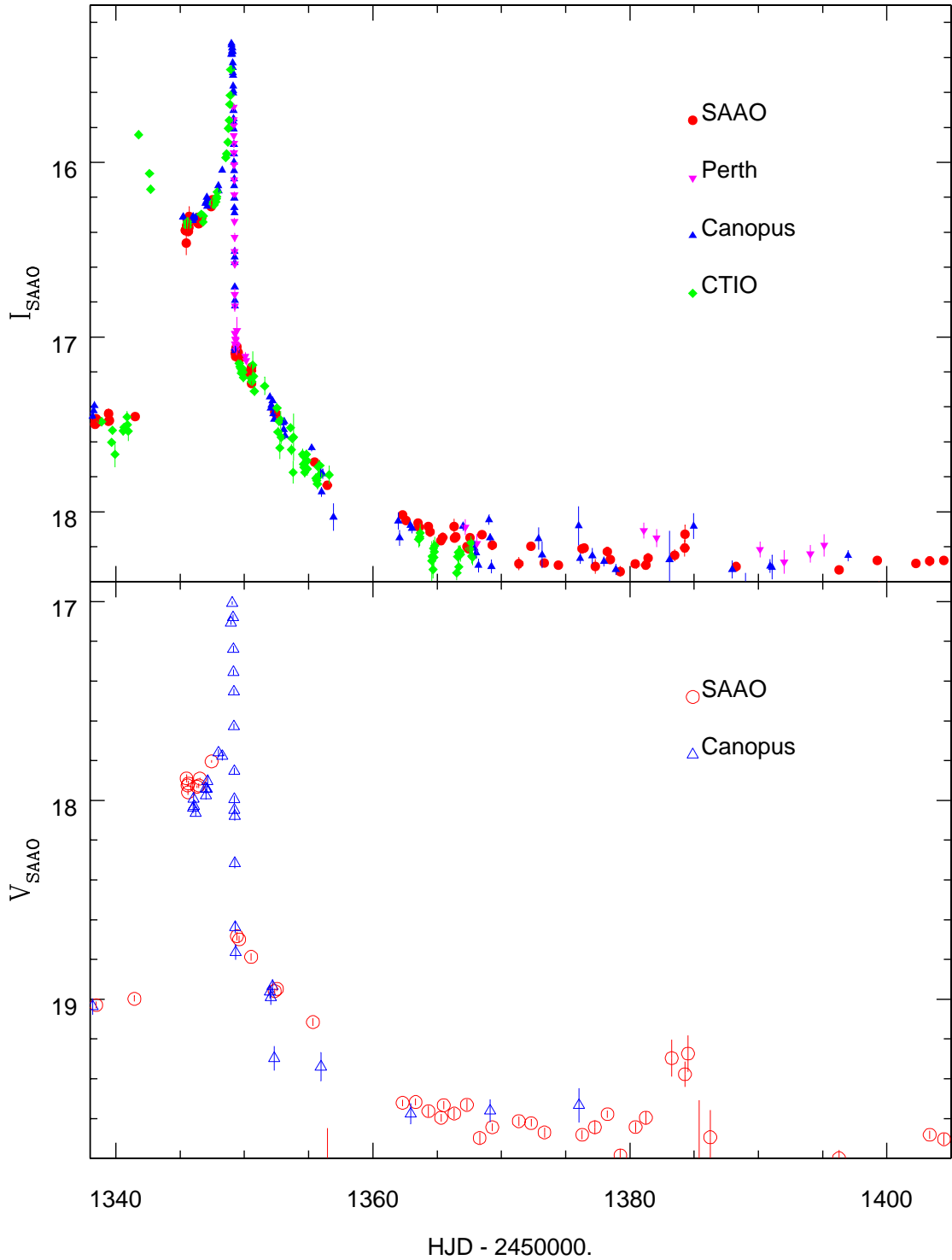


Fig. 1.— Whole data set excluding later-time baseline points ( $1338 < \text{HJD}' < 1405$ ), in I (upper) and V (lower) bands. Only the zero points of the different instrumental magnitude systems have been aligned using the result of the caustic crossing fit (§2.2); no attempt has been made to account for either different amounts of blended light or seeing corrections.

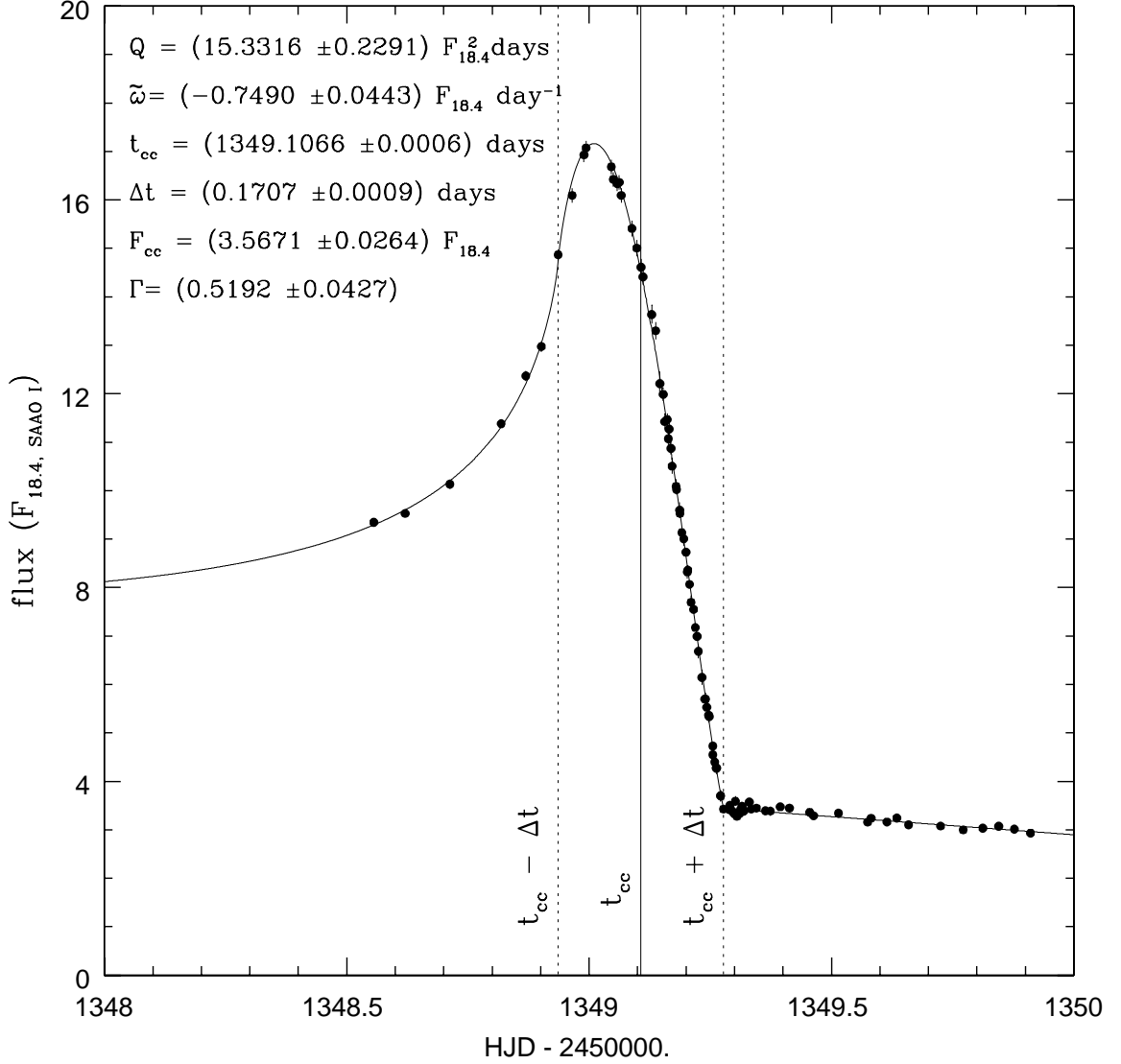


Fig. 2.— Fit of the caustic-crossing data to the six-parameter analytic curve given by eq. (1). The time of second caustic crossing ( $t_{cc}$ ) and the time scale of caustic crossing ( $\Delta t$ ) are indicated by vertical lines. The instrumental SAAO I-band flux,  $F_{18.4}$ , is given in units of the zero point  $I = 18.4$ .

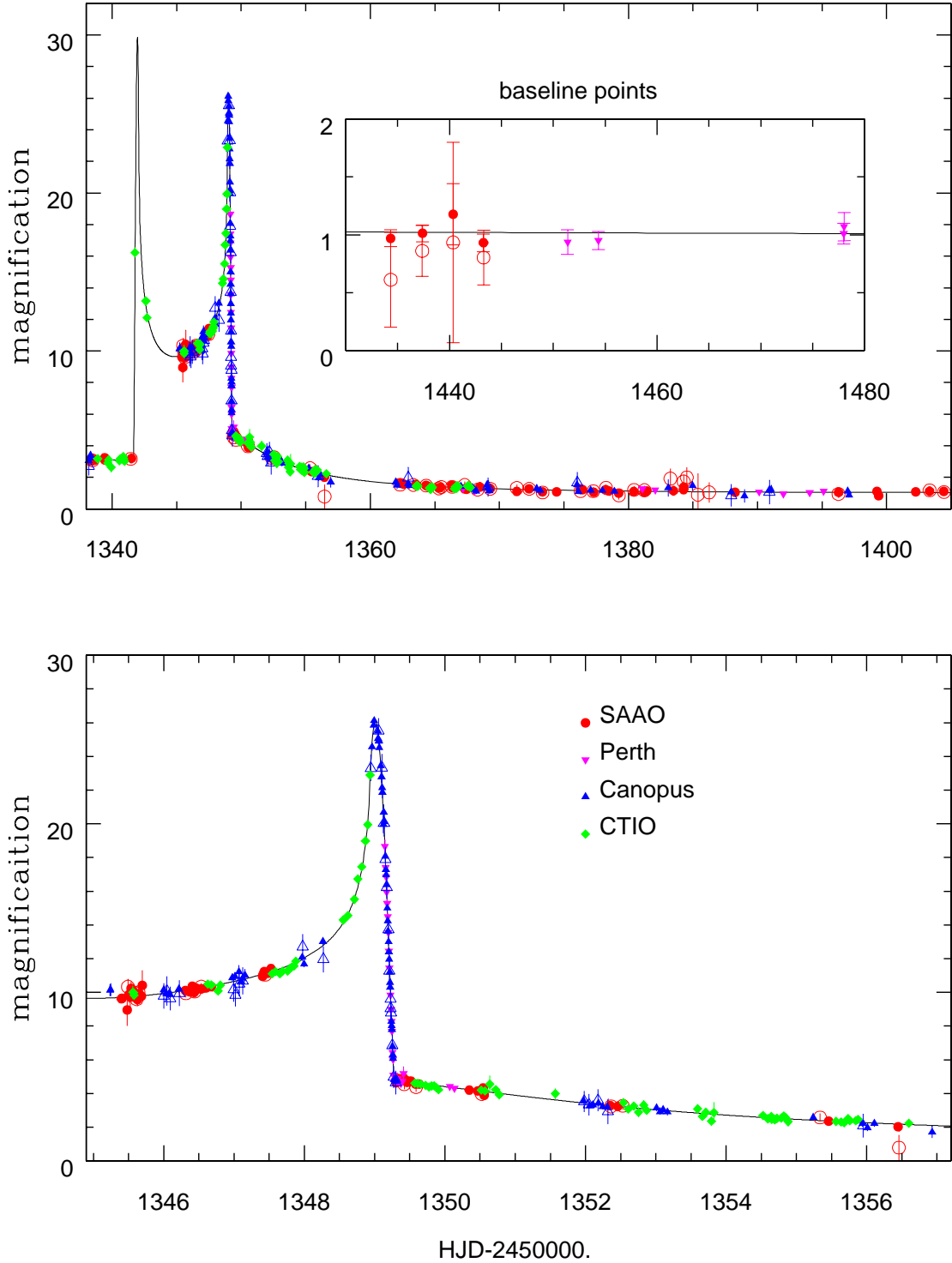


Fig. 3.— Magnification curve of the best-fit model taken from Table 2 for  $(d, q) = (2.42, 0.39)$ . Data included are SAAO (*circles*), Perth (*inverted triangles*), Canopus (*triangles*), and CTIO (*diamonds*). Closed symbols are for I band, and open symbols are for V band. Lower panel is a close-up of the time interval surrounding the second caustic crossing.

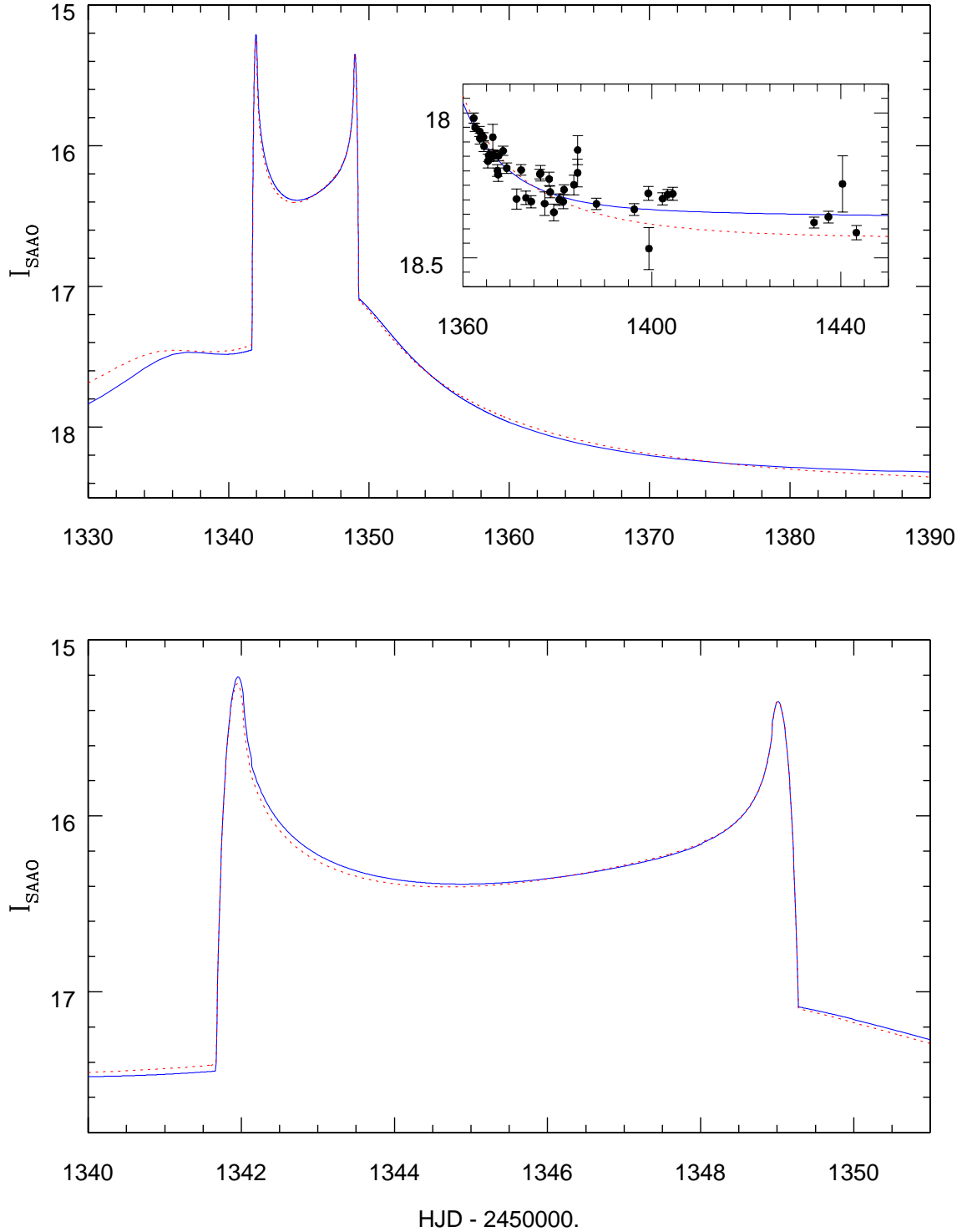


Fig. 4.— I-band light curves of the two “degenerate” models in SAO instrumental I magnitude. The solid line is the best-fit model of a wide binary lens,  $(d, q) = (2.42, 0.39)$ , and the dotted line is the close binary-lens model,  $(d, q) = (0.56, 0.56)$ . The filled circles are SAO data points. Both models are taken from Table 2 and use the estimates of blending factors and baselines. The upper panel is for the whole light curve covered by the data, and the lower panel is for the caustic-crossing part only.

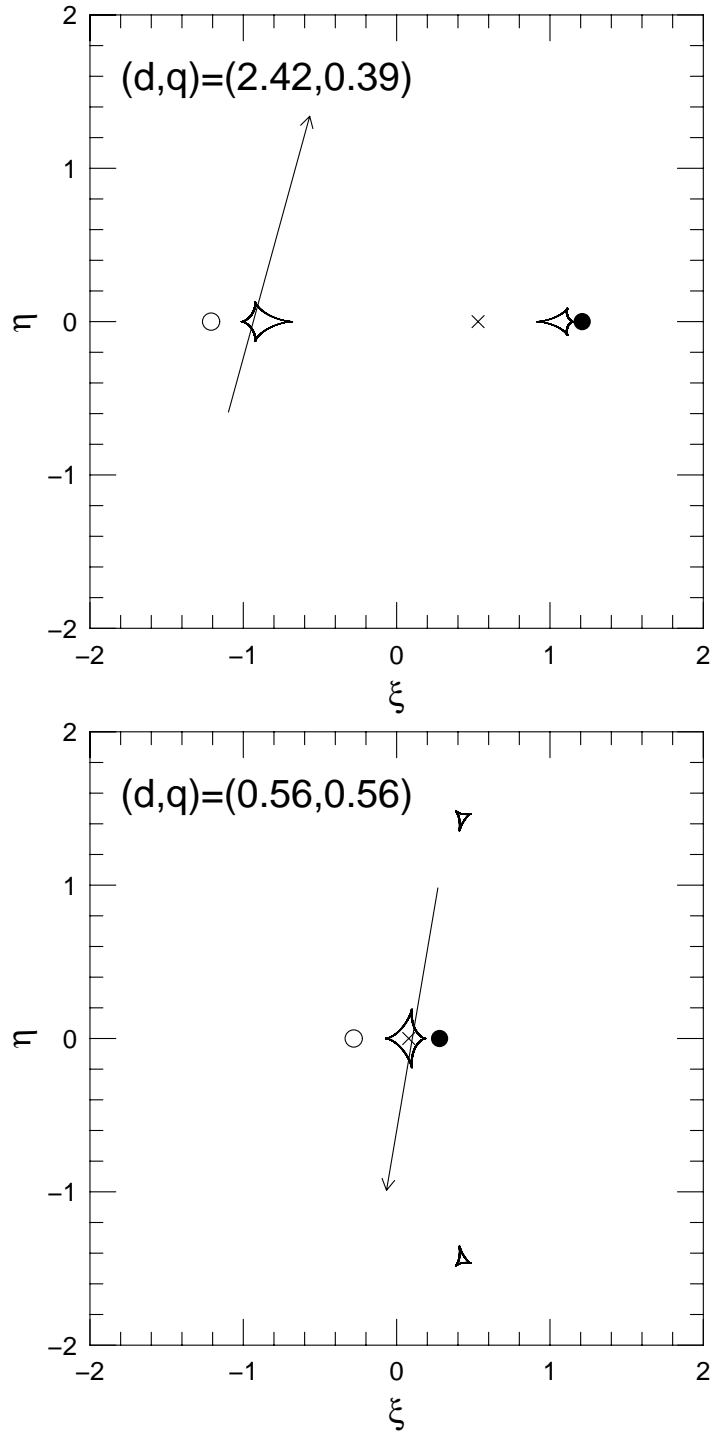


Fig. 5.— Lens geometries of the two “degenerate” models. The origin of the coordinate system is the geometric center of the binary lens, and ‘x’ is the center of the mass of the lens system. One unit of length corresponds to  $\theta_E$ . Closed curves are the caustics, the positions of the binary lens components are represented by circles, with the filled circle being the more massive component. The trajectory of the source relative to the lens system is shown by arrows, of which the lengths are  $2\theta_E$ .

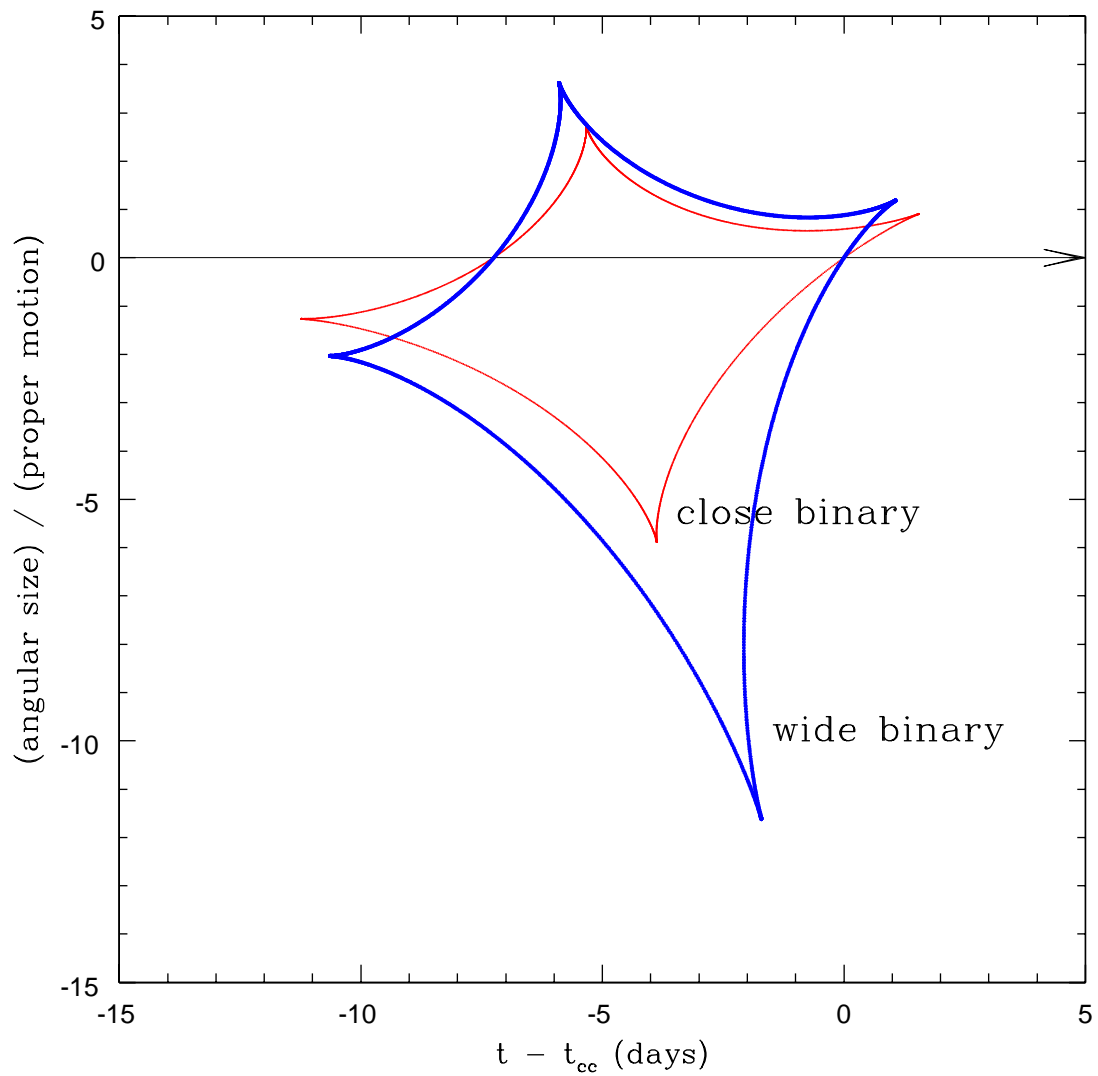


Fig. 6.— Caustics of the two “degenerate” models with respect to the source path shown as a horizontal line. The similarity of the light curves seen in Fig. 4 is due to the similar morphology of the caustics shown here.

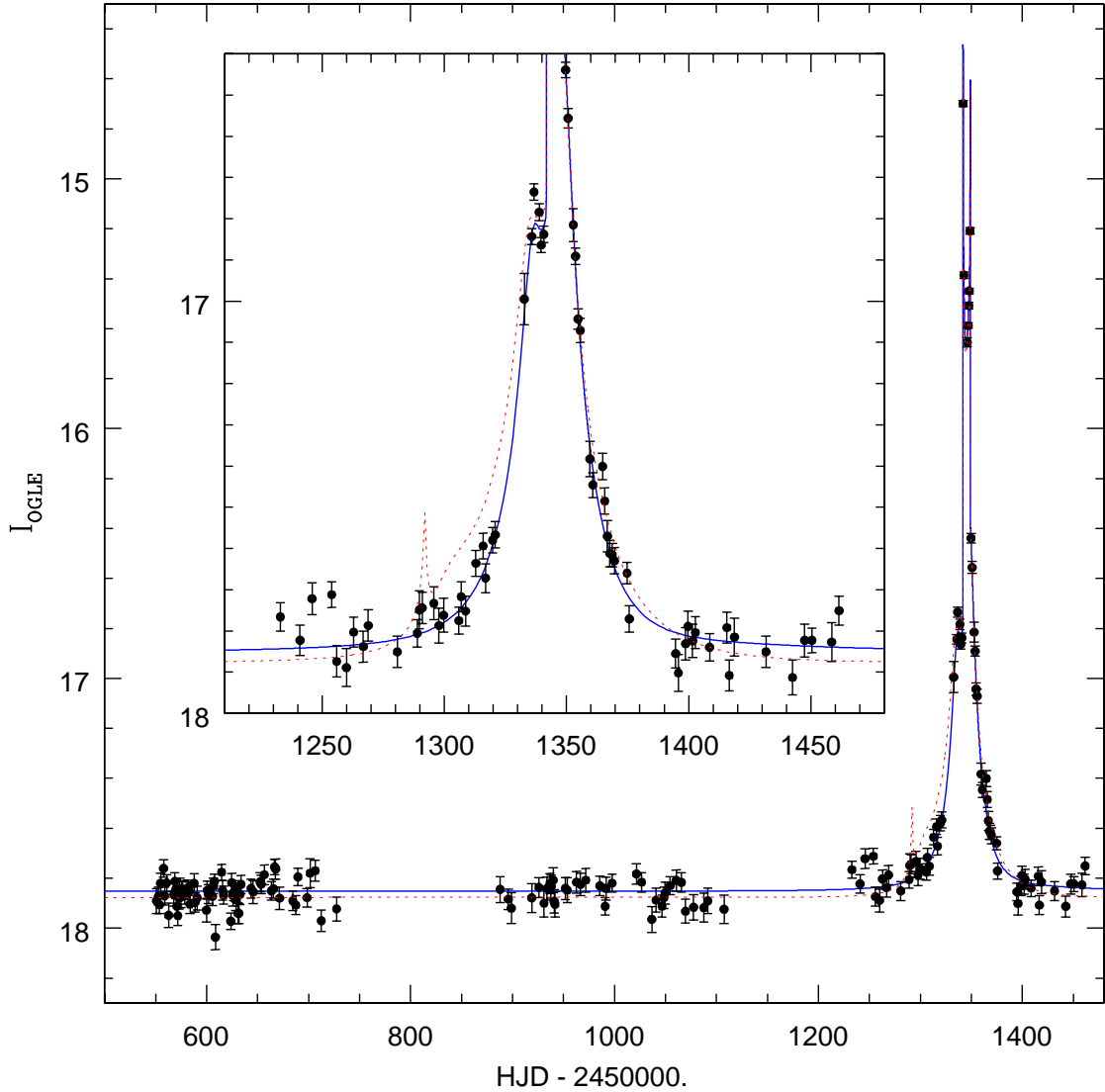


Fig. 7.— OGLE observations of OGLE-1999-BUL-23. The solid line is the light curve of the best-fit PLANET model (wide w/LD), and the dotted line is the PLANET close binary model (close w/LD). The models are determined by fitting PLANET data only, but the agreement between the PLANET model (wide w/LD) and OGLE data is quite good. On the other hand, OGLE data discriminate between the two “degenerate” PLANET models so that the wide-binary model is very much favored, in particular, by the observations in  $(1250 < \text{HJD}' < 1330)$ . The baseline of the PLANET model (wide w/LD) is,  $I_{OGLE} = 17.852 \pm 0.003$ , which is consistent with the value reported by OGLE,  $I_{OGLE} = 17.850 \pm 0.024$ .

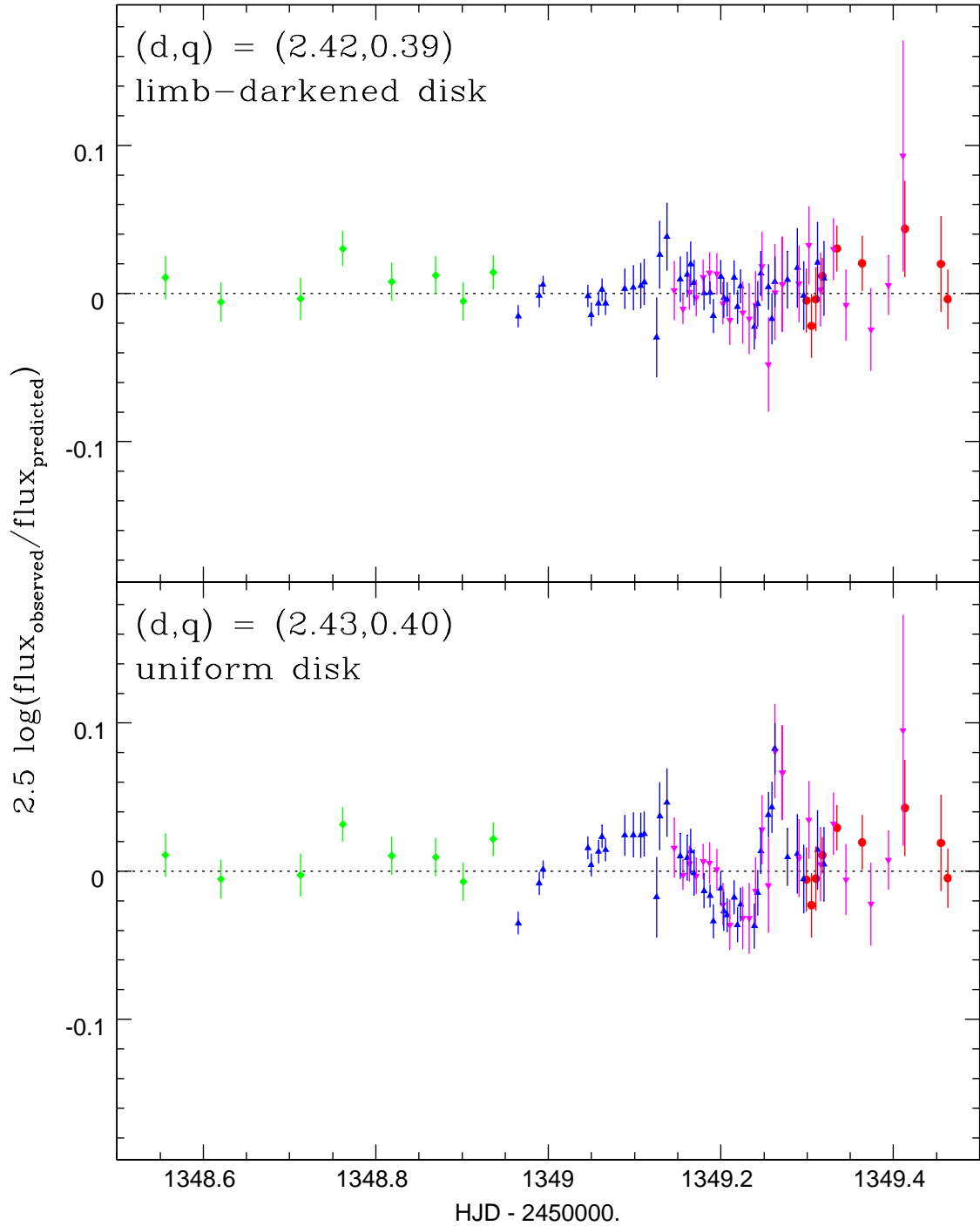


Fig. 8.— Residuals from PLANET models of OGLE-1999-BUL-23 around the second caustic crossing. Upper panel shows the residual for a model incorporating linear limb darkening (wide w/LD) and lower panel shows the same for a uniform disk model (wide no-LD). Both models are taken from Table 2. Symbols are the same as in Fig. 3. The residuals from the uniform disk are consistent with the prediction that the source is limb-darkened while the remaining departures from the limb-darkened model – which are marginally significant – may be due to non-linearity in the surface brightness profile of the source star.

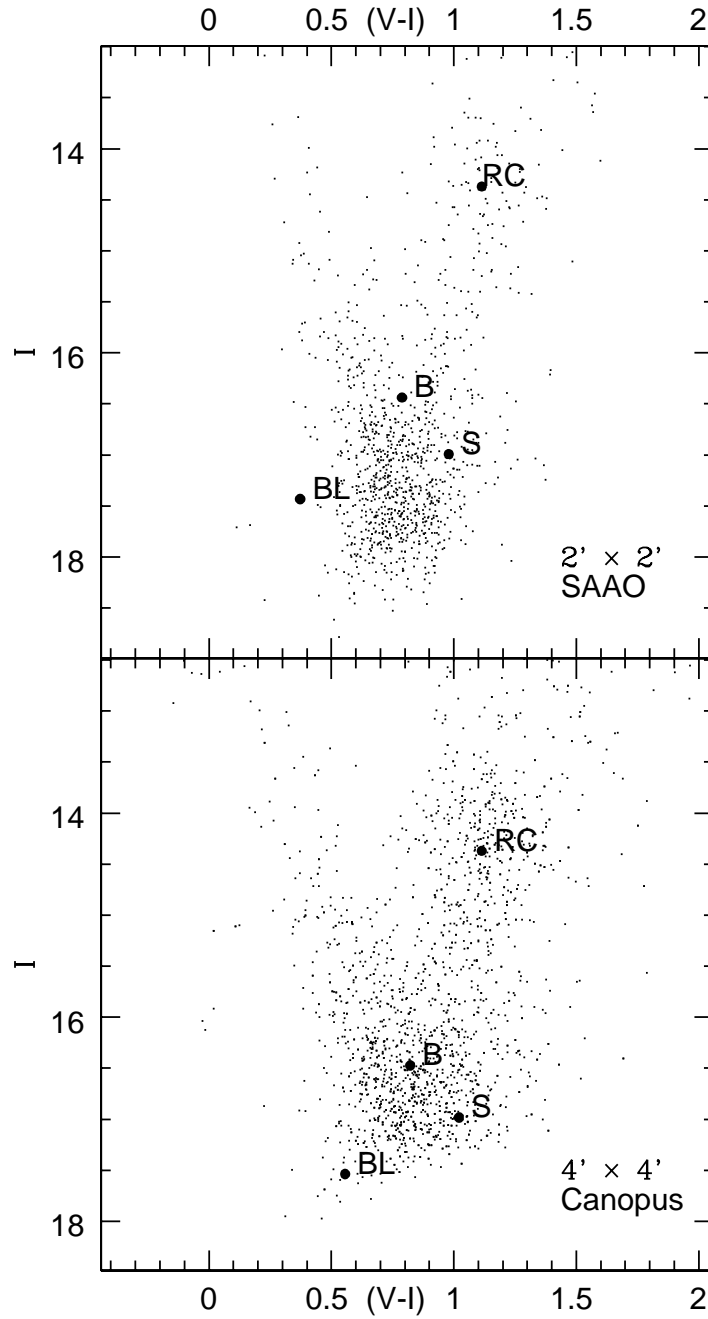


Fig. 9.— Color-magnitude diagram (CMD) of the field centered on OGLE-1999-BUL-23. Upper CMD is derived from  $2' \times 2'$  SAAO images, and lower CMD is from  $4' \times 4'$  Canopus images. The positions of the unlensed source (S), the baseline (B), blended light (BL) at median seeing, and the center of red clump giants (RC), are also shown. The extinction inferred from the (reddened) OGLE magnitude of the source in the I band is,  $A_I = 1.18$ , which implies  $E(V - I) = 0.792$  assuming the extinction law,  $A_I = 1.49E(V - I)$ .

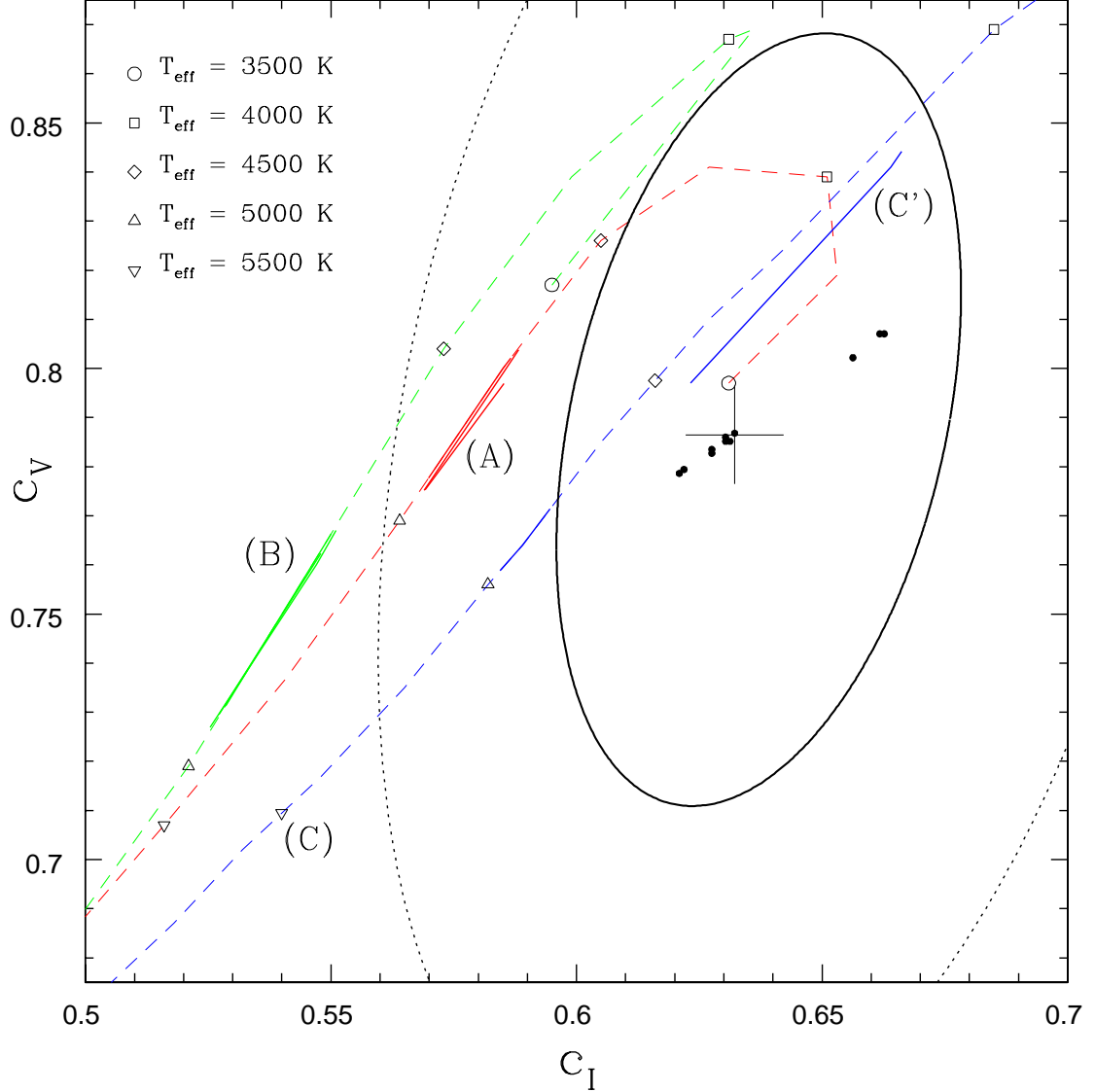


Fig. 10.— Comparison of linear limb-darkening coefficients. The measured value from the best model is represented by a small cross. One (*solid line*) and two (*dotted line*)  $\sigma$  error ellipses are also shown. Small dots are the results with different global parameters taken from Table 3. Various model predictions are displayed by dashed lines ( $\log g = 3.5$ ). Model (A) is taken from Díaz-Cordovés et al. (1995) and Claret et al. (1995), (B) is from van Hamme (1993), and (C) is from Claret (1998b). In particular, the predicted values in the temperature range that is consistent with our color measurements ( $T_{\text{eff}} = [4820 \pm 110]$  K for  $\log g = 3.0$ ;  $T_{\text{eff}} = [4830 \pm 100]$  K for  $\log g = 3.5$ ; and  $T_{\text{eff}} = [4850 \pm 100]$  K for  $\log g = 4.0$ ) are emphasized by thick solid lines. Model (C') is by Claret (1998b) for stars of  $T_{\text{eff}} = (4850 \pm 100)$  K for  $\log g = 4.0$ . Although the measured value of the limb-darkening coefficients alone favors this model, the model is inconsistent with our estimation of the proper motion.

This figure "f6c.gif" is available in "gif" format from:

<http://arxiv.org/ps/astro-ph/0004243v2>